

Insights to unusual antiferromagnetic behavior and exchange coupling interactions in $Mn_{23}C_6$

Ze-Kun Yu(于泽坤), Chao Zhou(周超), Kuo Bao(包括), Zhao-Qing Wang(王兆卿), En-Xuan Li(李恩萱), Jin-Ming Zhu(朱金铭), Yuan Qin(秦源), Yu-Han Meng(孟钰涵), Pin-Wen Zhu(朱品文), Qiang Tao(陶强), and Tian Cui(崔田)

Citation: Chin. Phys. B, 2025, 34 (**3**): 037101. DOI: 10.1088/1674-1056/adaadd
Journal homepage: http://cpb.iphy.ac.cn; http://iopscience.iop.org/cpb

What follows is a list of articles you may be interested in

Electronic band structures of topological kagome materials

Man Li(李满), Huan Ma(马欢), Rui Lou(娄睿), and Shancai Wang(王善才)
Chin. Phys. B, 2025, 34 (**1**): 017101. DOI: 10.1088/1674-1056/ad925d

Simultaneous control of ferromagnetism and ferroelasticity by oxygen octahedral backbone stretching

Genhao Liang(梁根豪), Hui Cao(曹慧), Long Cheng(成龙), Junkun Zha(查君坤), Mingrui Bao(保明睿), Fei Ye(叶飞), Hua Zhou(周华), Aidi Zhao(赵爱迪), and Xiaofang Zhai(翟晓芳)
Chin. Phys. B, 2024, 33 (**9**): 097101. DOI: 10.1088/1674-1056/ad553c

Two-dimensional Sb net generated nontrivial topological states in $SmAgSb_2$ probed by quantum oscillations

Jian Yuan(袁健), Xian-Biao Shi(石贤彪), Hong Du(杜红), Tian Li(李田), Chuan-Ying Xi(郗传英), Xia Wang(王霞), Wei Xia(夏威), Bao-Tian Wang(王保田), Rui-Dan Zhong(钟瑞丹), and Yan-Feng Guo(郭艳峰)
Chin. Phys. B, 2024, 33 (**7**): 077102. DOI: 10.1088/1674-1056/ad4bc2

Magnetism, heat capacity, magnetocaloric effect, and magneto-transport properties of heavy fermion antiferromagnet CeGaSi

Li-Bo Zhang(张黎博), Qing-Xin Dong(董庆新), Jian-Li Bai(白建利), Qiao-Yu Liu(刘乔宇), Jing-Wen Cheng(程靖雯), Cun-Dong Li(李存东), Pin-Yu Liu(刘品宇), Ying-Rui Sun(孙英睿), Yu Huang(黄宇), Zhi-An Ren(任治安), and Gen-Fu Chen(陈根富)
Chin. Phys. B, 2024, 33 (**6**): 067101. DOI: 10.1088/1674-1056/ad3060

High-temperature ferromagnetism and strong π-conjugation feature in two-dimensional manganese tetranitride

Ming Yan(闫明), Zhi-Yuan Xie(谢志远), and Miao Gao(高淼)
Chin. Phys. B, 2023, 32 (**3**): 037104. DOI: 10.1088/1674-1056/acae7b

---

SPECIAL TOPIC — Structures and properties of materials under high pressure

Insights to unusual antiferromagnetic behavior and exchange coupling interactions in $Mn_{23}C_6$

Ze-Kun Yu(于泽坤)[1], Chao Zhou(周超)[1], Kuo Bao(包括)[1,†], Zhao-Qing Wang(王兆卿)[1], En-Xuan Li(李恩萱)[1], Jin-Ming Zhu(朱金铭)[1], Yuan Qin(秦源)[1], Yu-Han Meng(孟钰涵)[1], Pin-Wen Zhu(朱品文)[1], Qiang Tao(陶强)[1], and Tian Cui(崔田)[1,2,‡]

[1] *State Key Laboratory of Superhard Materials, College of Physics, Jilin University, Changchun* 130012, *China*
[2] *Institute of High Pressure Physics, School of Physical Science and Technology, Ningbo University, Ningbo* 315211, *China*

(Received 10 October 2024; revised manuscript received 13 January 2025; accepted manuscript online 16 January 2025)

We report the structural, mechanical and electromagnetic properties of the intermetallic compound $Mn_{23}C_6$. The bulk $Mn_{23}C_6$ sample was synthesized using high temperature high pressure quenching method (HTHPQM), and investigated in detail by x-ray diffraction, electron microscope, magnetization and electrical resistivity measurements, etc. First-principles calculation based on density functional theory *ab intio* simulation was carried out to calculate the bonding and electromagnetic properties of $Mn_{23}C_6$. Based on our experimental and simulated results, the $Mn_{23}C_6$ in this work is single phase of a faced-centered cubic structure with space group *Fm*-3*m* (No. 225). Determined by SEM and TEM, the bulk sample consists of monocrystal $Mn_{23}C_6$ crystals with 2–15 μm grain sizes, it is the quick quenching method in the synthesizing process that brings such small crystal grain size. Archimedes method gives its density of 7.14 g/cm^3, 95.74% of its theoretically calculated density 7.458 g/cm^3. Owing to the abundant Mn 3d electrons and a framework of strongly linked Mn atoms in $Mn_{23}C_6$, the electrical conductivity is up to 8.47×10^{-4} Ω·m, which shows that $Mn_{23}C_6$ is a good conductor. Our magnetic susceptibility analyses reveal a magnetization peak in the *M*–*T* curve at 104 K, combined with the *M*–*H* curve and Curie–Weiss law, this peak usually means the transformation between paramagnetic and antiferromagnetic orders. To gain an insight into the mechanism of the magnetic phase transition, we calculated the magnetic properties, and the results show that different from normal antiferromagnetic order, the magnetic orders in $Mn_{23}C_6$ consist of three parts, the direct ferromagnetic and antiferromagnetic exchange coupling interactions between Mn atoms, and the indirect antiferromagnetic super-exchange interaction between Mn and C atoms. Therefore, we reveal that the $Mn_{23}C_6$ is a complex magnetic competition system including different magnetic orders and interactions, instead of the normal long-range antiferromagnetic order.

Keywords: intermetallic compound (IMC), magnetism, high temperature high pressure (HTHP), density functional theory (DFT)

PACS: 71.20.Lp, 91.60.Pn, 71.15.Mb, 31.15.eg

DOI: 10.1088/1674-1056/adaadd **CSTR:** 32038.14.CPB.adaadd

1. Introduction

The precipitation of intermetallic compound (IMC) in magnet steels or other wear and corrosion resistance steels is of great technological importance as the IMC dramatically influences several mechanical properties of these materials.[1–3] Owing to their specific atomic radius ratio, Mn elements and C elements can form abundant binary IMCs with a series of specific Mn/C coordination numbers.[4] In the family of binary IMCs, the precipitation order of binary carbides usually follows the rule that $M_3C \rightarrow M_7C_3 \rightarrow M_{23}C_6$ (*M*: transition metal elements, such as Ti, V, Cr, Mn and Fe),[5] and $M_{23}C_6$ is confirmed to be the most stable carbide.[6–8] As a typical IMC and has been found in different magnet steels and Ni-base superalloys,[9,10] $Mn_{23}C_6$ has received a lot of attention, especially to the electromagnetic properties. Comprehending the properties and mechanisms of $Mn_{23}C_6$ is important for relevant material applications.

The pioneer of systematic research $Mn_{23}C_6$ in steels is Morgan,[11] who found that $Mn_{23}C_6$ is non-magnetic order at ambient temperature. It appears very weak ferromagnetism in manganese-rich alloy $Mn_{79}In_1C_{20}$, and the ferromagnetism gradually enhances with the increase of indium from 0 to 20 pts. These indicate that the magnetic orders of $Mn_{23}C_6$ are intricate and complex. To figure out the magnetic order, Benz, Elliot, and Chipman[12,13] calculated the dynamic phenomena and thermodynamics of all potential manganese carbides, and Karen *et al.*[14] measured their magnetic properties in experiments. These works indicate that only $Mn_{23}C_6$, Mn_5C_3 and Mn_7C_3 are thermodynamically stable at ambient temperatures, among them, measured by a Faraday balance and neutron diffraction, only $Mn_{23}C_6$ has magnetic order in all stable manganese carbides from 16 K to 300 K, and the mag-

†Corresponding author. E-mail: baokuo@jlu.edu.cn
‡Corresponding author. E-mail: cuitian@nbu.edu.cn

© 2025 Chinese Physical Society and IOP Publishing Ltd. All rights, including for text and data mining, AI training, and similar technologies, are reserved.

netic susceptibility of $Mn_{23}C_6$ is weak paramagnetic at ambient temperature, instead of non-magnetic order like before. With temperature decreases to 104 K, a Curie–Weiss behavior is observed with $\Theta_p = 38 \pm 3$ K, and $\mu_{eff} = 1.46 \pm 0.02\ \mu_B$, means that the magnetic order is antiferromagnetic. These results confirm that the magnetism of $Mn_{23}C_6$ is antiferromagnetism in macroscopic, however, it is also unable to explain the mechanism for the occurrence of ferromagnetism in manganese-rich alloy like $Mn_{80-x}In_xC_{20}$,[11] thus it is still lack of observation in microscopic. Until the recent decades, with the rapid development of highly sensitive magnetic detection equipment represented by superconducting quantum interference device (SQUID)[15] and x-ray magnetic circular dichroism (XMCD),[16] it is possible to analyze magnetism with high precision in microscopic. With the help of sophisticated equipments, Guchhait *et al.*[17] measured the magnetic order of $Mn_{23}C_6$ both in macro and micro scopes. The results show that $Mn_{23}C_6$ ought to be antiferromagnetic with a Néel temperature T_N of about 105 K, which is the same as the results of Karen *et al.*[4] before, but they also found a very weak ferromagnetic signal when temperature was below 100 K. It is worth noting that this weak ferromagnetic signal indicates that only about 1 pts of Mn atoms are in ferromagnetic order in $Mn_{23}C_6$.

Based on the above researches, the magnetic orders of $Mn_{23}C_6$ include at least two magnetic exchange interactions, the strong antiferromagnetic exchange interactions and the weak ferromagnetic exchange interactions. This means that $Mn_{23}C_6$ is not antiferromagnetic in the traditional sense. While the crystallography and magnetism of $Mn_{23}C_6$ were studied in many works,[11–14,17] there is still quite much insufficient information and incomplete understanding on the mechanisms. Due to that the magnetic measurements usually require a large number of samples, this is partly related to the difficulty to synthesize bulk monolithic $Mn_{23}C_6$. To figure out the magnetic properties and the underlying physics thoroughly, through a combination of experimental measurements and *ab intio* density functional theory (DFT) calculations,[18] we studied the structural, mechanical, and electromagnetic properties of $Mn_{23}C_6$ systematically. Our work resolves the long-standing question of the magnetic exchange interactions in $Mn_{23}C_6$, and this work would also provide a guidance in underlying physics and broaden understanding of $Mn_{23}C_6$.

2. Sample synthesis

2.1. High temperature and high pressure quenching method

The high temperature and high pressure quenching method (HTHPQM) is based on the large volume–high static pressure (LVP). Compared with other normal synthetic methods, due to the introduction of high pressure and quick quenching techniques, HTHPQM can provide relatively higher hydrostatic pressure environment in material synthesis and intercept the metastable phase of material from extreme conditions, therefore it has great influence in the high pressure areas of scientific and technological researches. The LVP we used in this work is a cubic-anvil high pressure apparatus (model: SPD 6×14400 N, G. Y. MACHINERY Co., Ltd.), the main components of the cubic-anvil high pressure apparatus include two basic parts: anvil and cubic sample cell, and Fig. S1 of the supplementary material illustrates the structure of the cubic-anvil high pressure apparatus, which consists of six anvils coupled to independent hydraulic cylinders surrounding a cubic sample cell. The anvil is cobalt-cemented tungsten carbide with a square anvil face size of 23.5×23.5 mm, and each anvil has a water-cooling system to prevent thermal dissipation damage from heating the sample. All anvils are driven by a hydraulic pump to generate high pressure and heating sample through a few hundred Amperes of current. The detailed compositions of the cubic sample cell are shown in Fig. S2 of the supplementary material.

2.2. Sample preparation and fabrication

We synthesized polycrystalline bulk $Mn_{23}C_6$ by using HTHPQM in the six-anvil press (SPD 6×14400 N). The sample precursor was pre-processed by mixing the Mn powder (Alpha Co., Ltd., CAS: 7439-96-5; APS 50–100 μm, purity 99.6%) and C powder (Aladdin Scientific Corp., CAS: 7782-42-5; APS 1–5 μm, purity 99.95%) with its stoichiometric molar ratio and grinding those powders in an agate mortar (Φ50 mm) for 4 hours. We then weighed 18 mg precursor powder approximately and poured this mixing powder into a vertical cylindrical die with a diameter and height of 4.0 mm and 2.5 mm, respectively. Thereafter, squeezed the die on 1 MPa pressure and held for 60 s so that the precursor powder became a wafer. Assembled this wafer with a series of parts, and put those into the six-anvil press and carried out the synthesis. The temperature and pressure for synthesis were 1200 K and 5.0 GPa, respectively. The sample was holden under these conditions for 30 min and then quenched to room temperature at an approximate cooling rate of 200 K/s.

3. Experiment and simulation details

3.1. Experimental proceeding

X-ray diffraction was conducted using the XtaLAB synergy custom system (Rigaku Corp. Inc.). $Mn_{23}C_6$ emitted strong secondary radiation when using a Cu target, so spectra were acquired using a Mo target. The sample was tested by using a high-flux rotating anode x-ray source (FR-X) with a power of 2.97 kW and integration time of 60 s at room temperature and ambient pressure. Data refinement was conducted

using the Rietveld method and Le Bail method in the General Structure Analysis System (GSAS)[19] software package. The crystal structure parameters were obtained from the Inorganic Crystal Structure Database (ICSD) with collection code 69536. Density data were obtained by Archimedes method.

Structural and morphological characterizations were carried out using the Magellan 400 (XHR) SEM (Field Electron and Ion Co.), with EDS microanalysis using an Ultim Max silicon drift detector and Aztec system (Oxford Instruments Plc.). The acquisition parameters were as follows: spot size, 3 nm; accelerating voltage, 3.00 kV; current, 25 pA; working distance, 3.8 mm; and detector mode, ETD.

The temperature dependent magnetic susceptibility and hysteresis loops were measured using physical property measurement system and superconducting quantum interference device-vibrating sample magnetometer (Quantum Design Co., Ltd.). Electronic conductivity measurements were carried out on a source measure unit (Tektronix, Inc., 2450 Source Meter) based on the Kelvin method.

3.2. DFT simulation

The *ab initio* structural relaxations and electromagnetic property calculations were performed within the framework of spin-polarized density functional theory (DFT)[18] using the Vienna *Ab-initio* Simulation Package (VASP).[20–22] The electron–ion interaction was described by applying the projector augmented wave (PAW)[23] method, which was adopted with $3s^2 3p^6 3d^6 4s^1$ and $2s^2 2p^1$ as the valance electrons for Mn and C atoms, respectively. The Perdew–Burke–Ernzerhof (PBE) functional within the generalized gradient approximation (GGA)[24] was implemented for the exchange–correlation functional. An energy cut-off 600 eV for the plane-wave basis, a dense Mokhorst–Pack[25] k-points grids of $7 \times 5 \times 3$ and Monkhorst–Pack k-mesh spacing of $2\pi \times 0.03$ Å^{-1} were used in the calculations, which ensures that the total energies are well converged to better than 1 meV per formula unit (f.u.). The forces between the atoms converged to within 0.01 eV/Å in the relaxation. To calculate the magnetic moments, the parallel state as the representative magnetic configuration was considered. The parallel state used the wavefunction $\langle \chi_1 \rangle_{i,i+1} = \langle \psi \rangle_i + \langle \psi \rangle_{i+1,i} = 1, 3, \ldots, 13$. Based on all above, we studied density of states (DOS), electron localization function (ELF), spin–polarized electron (SPe), projected crystal orbital Hamilton population (pCOHP), etc., and analyzed them with experimental results to deeply understand the material properties.

3.3. Drafting and illustration

As citing request and policy from the institutions about relative software packages, here we list the data processing and drafting softwares used in this paper. Among these softwares, EXPGUI[26] developed by Toby is used in crystallographic structure refinement process, VESTA[27] development by Momma and Izumi is used in 3D visualization of crystalline and electronic structures plots.

4. Results and discussion

In this paper, we synthesized bulk sample $Mn_{23}C_6$ by means of HTHPQM at 5.0 GPa and 1200 K in a cubic-anvil high pressure apparatus using Mn and C powders as the precursors, the detailed preparation process is shown in the sample preparation and fabrication section of supplementary material. Figure 1(a) showcases powder x-ray diffraction (XRD) and its Rietveld refinement, these confirmed that the single phase polycrystalline $Mn_{23}C_6$ has a faced-centered cubic (FCC) structure with space group $Fm\text{-}3m$ (No. 225) and the strukturbericht symbolism is the $D8_4$ structure, the diffraction pattern matches well with the existing reference from the inorganic crystal structure database (ICSD, Coll. code: 69536) (see Table S1 in the supplementary material). The lattice parameter we calculated is $a = b = c = 1.0415$ nm, an $Mn_{23}C_6$ unit cell contains 116 atoms, including 92 Mn atoms in four different Wyckoff positions and 24 C atoms in only one Wyckoff position.

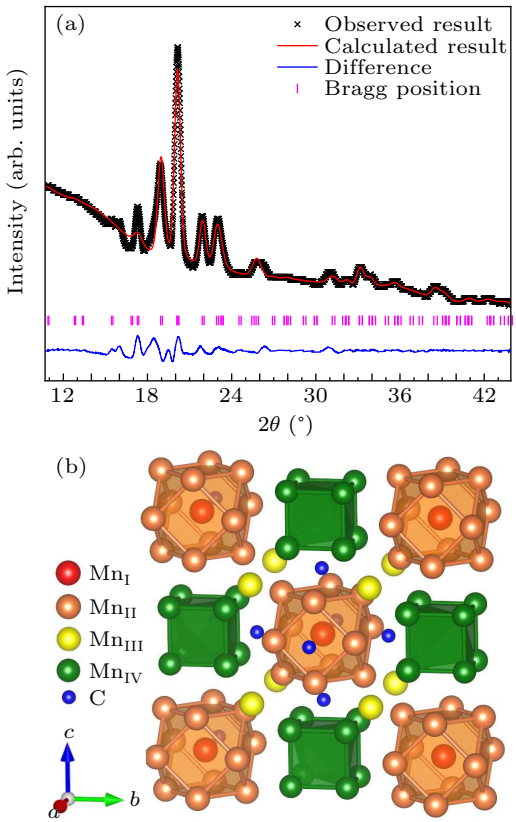


Fig. 1. (a) Powder x-ray diffraction and Rietveld refinement of $Mn_{23}C_6$ polycrystalline produced by HTHPQM: black cross symbol, red line, blue line and pink main string are observed result, calculated result, difference and Bragg position, respectively. (b) The crystal structure of $Mn_{23}C_6$, smaller blue balls are C atoms, other bigger balls with different colors represent Mn atoms at different Wyckoff positions.

The three-dimensional crystal structure of $Mn_{23}C_6$ is presented in Fig. 1(b), it has a typical crystal structure of the $M_{23}C_6$-type (M: transition metal elements) based on the FCC lattice (the $cF116$ crystallography notation in the Pearson symbol). $Mn_{23}C_6$ as a typical IMC, its crystal structure is often described as made up of the packing of some coordination polyhedral, cubo-octahedra and cubes. The cubo-octahedron (orange polyhedrons in Fig. 1(b)) is formed by 12 Mn_{II} atoms in 48h sites and one central Mn_I atom in the 4a site, while the cube (green polyhedrons in Fig. 1(b)) is formed by 8 Mn_{IV} atoms in 32f sites. In addition, cubo-octahedra are allocated to the face-centered cubic lattice points (i.e., 4e sites) while cubes are allocated to the centers of octahedral gaps formed by six cubo-octahedra (i.e., to mid-points of the cube edge and the body center of the lattice). Such complex structure and many atoms in a unit cell bring a great challenge to synthesis and analysis, especially in DFT *ab intio* simulations.

To investigate the micro-morphology, we separate the sample and carry out the typical scanning electron microscopy (SEM) on the sliver fracture surface of polycrystalline $Mn_{23}C_6$ specimen. In Fig. 2(a), the average $Mn_{23}C_6$ crystal grain size is 2–15 μm, such small crystal grain is due to the fast quenching speed in the synthesizing process of HTHPQM. In the fast quenching process, the precursor quickly cools from high temperature, therefore there is not enough time for the crystal nucleus to grow large.[28] Besides, high pressure also limits the atomic average free path and further restricts crystal nucleus growth.[29–31] All above factors hold the atoms to form millimeter-scale long-range orders, which finally leads to the small crystal grain size of $Mn_{23}C_6$. These general grain refinement processes are like hardening and quenching processes in steels, which usually improve the mechanical properties of steels, but due to the presence of grain boundary gaps in grain refinement processes, the density of the material is usually reduced. But different from the above general grain refinement processes, our density measurement shows that the specimen density is about 7.14 g·cm^{-3} with the Archimedes method, which is 95.74% of the theoretical density of 7.458 g·cm^{-3}. Compared with other quenching processes,[9,32] the high relative density is due to the influence of high pressure reducing the distance between different atoms in the synthesizing process, therefore HTHPQM could natively reduce grain boundary gaps and enhance the density of $Mn_{23}C_6$. Such high density also agrees with the HRSEM image results in Figs. 2(b) and 2(d), the specimen fracture surface of $Mn_{23}C_6$ is homogeneous and it is almost free of visible micro-cracks and pores. In Fig. 2(c), the energy-dispersive x-ray spectroscopy (EDS) shows that Mn and C atoms are uniformly distributed on the

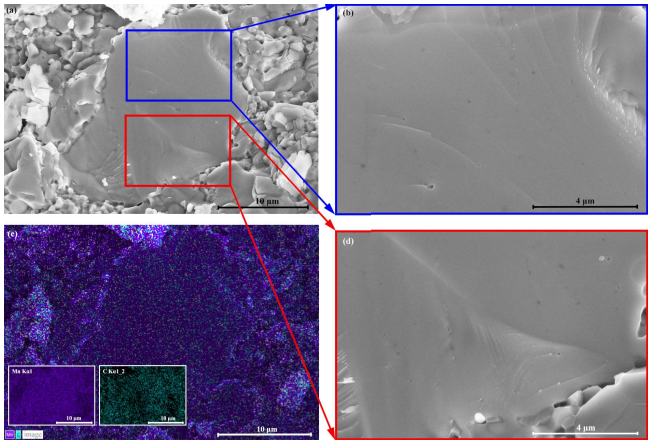


Fig. 2. The solid micro-morphology of $Mn_{23}C_6$ under magnification field-emission scanning electron microscope: (a) the low magnification image of a $Mn_{23}C_6$ single crystal; (b) and (d) the selected area high magnification images with different areas of (a); (c) the linear SEM-EDS results of Mn and C atoms in the area (a), the insets are the individual distribution patterns of Mn and C atoms, respectively.

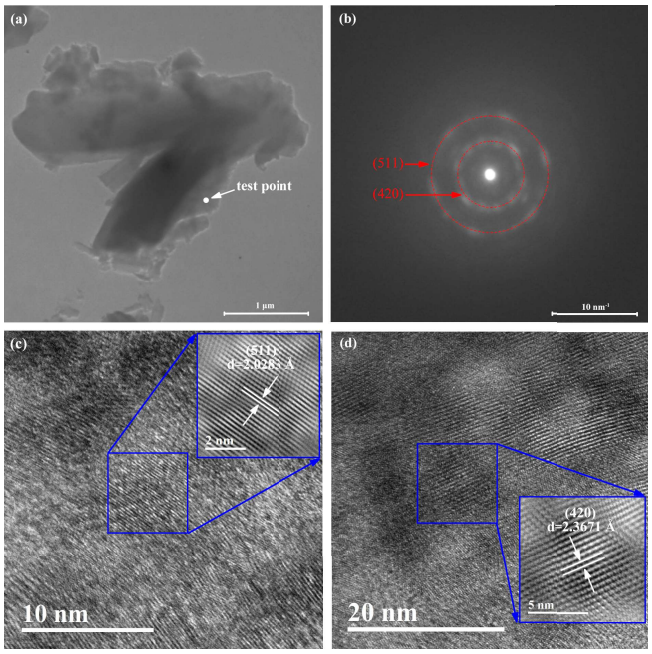


Fig. 3. Micro-morphology of $Mn_{23}C_6$ under transmission electron microscopy: (a) the bright-field image of $Mn_{23}C_6$; (b) the SAED image; (c) and (d) the HRTEM images.

surface of the $Mn_{23}C_6$ specimen without any significant aggregation and absence, which means that the sample is homogeneous and uniform. Besides that, we also study the transmission electron microscopy (TEM) images of nano-size specimens, and the results are presented in Fig. 3. To ensure electrons penetrate the specimen, we choose the suspension of $Mn_{23}C_6$ as the specimen, the nano-size specimen bright-field image is shown in Fig. 3(a). We take the edge of the nano-size specimen to get selected area electron diffraction (SAED) and high-resolution transmission electron microscope (HRTEM) images, the test point is marked in Fig. 3(a). Figure 3(b) shows the SAED image at the same scan area with Figs. 3(c) and 3(d). Different from the crystal diffraction spectra in Fig. 1(a),

figure 3(b) shows a typical quasi-crystal diffraction ring instead of a polycrystalline ring, this is due to the tiny spot size on the scale of nanometers and the minority nano-size specimens from $Mn_{23}C_6$ suspension. Figures 3(c) and 3(d) are the HRTEM images and their fast Fourier transform (FFT), which show that the lattice fringes are regular and neat, and means that $Mn_{23}C_6$ has good crystallization, almost without any visible dislocations or defects. Owing to the same scan area, the lattice plane in Figs. 3(c) and 3(d) also corresponds one-to-one to the lattice plane of the diffraction rings in Fig. 3(b). Combined with SEM, TEM and the previous powder XRD, these results demonstrate that the $Mn_{23}C_6$ synthesized by HTHPQM is single-phase, homogeneous and uniform. A high-quality $Mn_{23}C_6$ sample also ensures the reliability of subsequent measurements of electromagnetic properties.

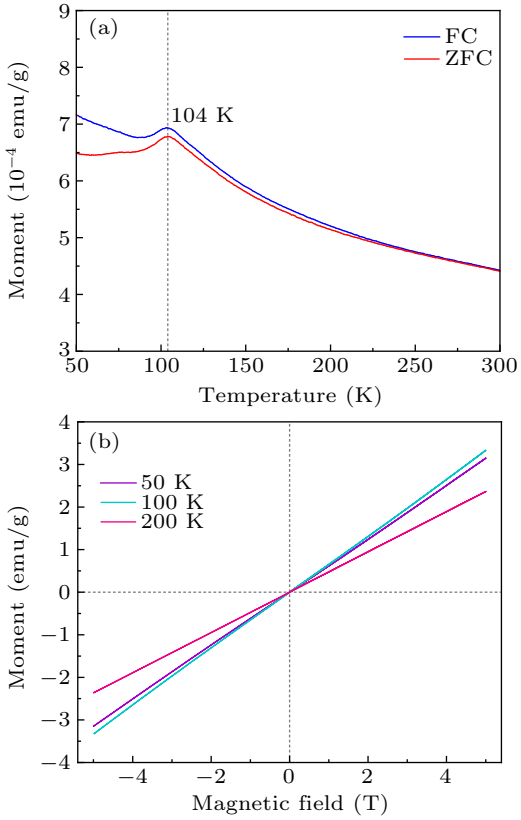


Fig. 4. The magnetizing process of $Mn_{23}C_6$: (a) the DC magnetization of moment versus temperature from 50 K to 300 K, the blue line and red line are field cooled (FC) and zero field cooled (ZFC) temperature dependence curves, respectively; (b) the hysteresis loops of moment versus magnetic field at 5 K, 10 K and 200 K.

Next, we investigate the magnetism of $Mn_{23}C_6$. Combining with the temperature dependence of the magnetic susceptibility (the *M*–*T* curve in Fig. 4(a)) and the temperature dependence hysteresis loops (the *M*–*H* curveint Fig. 4(b)), we reveal the magnetic properties at different temperatures and cooling conditions. In Fig. 4(a), the zero-field cooling (ZFC) and field cooling (FC) curves both increase monotonically with temperature decreasing from 300 K to 14 K, and show a magnetic transition peak at 14 K. Meanwhile, in Fig. 4(b), the slope of the *M*–*H* curve corresponding to 100 K is also the highest, according to the magnetism curves in Fig. 4 and previous research results,[14,17] we confirm that this is an antiferromagnetic phase transition, and 104 K is the Néel temperature of $Mn_{23}C_6$. Beyond that, there is a phenomenon here that has never been reported before, the ZFC and FC curves bifurcate when the temperature continuously decreases below 100 K. With temperature decreasing, the slopes of ZFC and FC are zero and positive, respectively. This bifurcated phenomenon in ZFC and FC usually means the existence of ferromagnetic–antiferromagnetic competition, magnetic cluster, spin frustration or fluctuations in this system.[33–36] Besides that, the resistivity test based on the Kelvin method shows that the resistivity of $Mn_{23}C_6$ at room temperature is about 8.47×10^{-4} Ω·m, which indicates that $Mn_{23}C_6$ is also an excellent electrical conductor among metallic carbides.

To gain an in-depth understanding of the electromagnetic properties, especially the unusual magnetic behavior, and figure out the inside exchange coupling interaction mechanisms of $Mn_{23}C_6$, we simulate the electromagnetic properties with *ab intio* DFT calculations. However, since the Mn atoms in $Mn_{23}C_6$ have four different Wyckoff positions and there are total 116 atoms in a unit cell, the crystal structure becomes very complicated. We take the initial lattice constants of $Mn_{23}C_6$ from our Rietveld refinement data in Table S1 of the supplementary material for simplified calculation. The electronic band structure, corresponding total density of states (TDOS) and partial density of states (PDOS) with spin polarized are shown in Fig. 5. Figure 5(a) gives the conduction band and the valence band overlap at the Fermi level (E_F), which indicates that $Mn_{23}C_6$ is metallic. The spin-up and spin-down both exist and noncoincidence, this implies that the magnetic order in the $Mn_{23}C_6$ system is complex. From the TDOS and PDOS in Fig. 5(b) and combined with the electronic band structures, the DOS around E_F are mostly contributed by Mn 3d electrons, similar to the result of the low resistivity in our experiment, the non-zero states at E_F in DOS also indicate the metallicity of $Mn_{23}C_6$. The upper and lower spins of Mn and C electrons both exist and are asymmetric, corresponding to the results of the previous *M*–*T* measurements, which indicates that the magnetic order comes from the coexistence of antiferromagnetism and ferromagnetism, and this is consistent with the previous research. Furthermore, there is a peculiar orbital hybridization between Mn 3d and C 2p orbitals within the range of −7.5 eV to −5.2 eV in Fig. 5(b), which suggests the existence of magnetic exchange interaction between Mn and C atoms. Figure 6 shows the electron localization function (ELF) for a unit cell and the (001) crystallographic plane of $Mn_{23}C_6$. The areas between Mn and C atoms are full of free electrons in Figs. 6(a) and 6(b), combined with DOS, these electrons are mostly contributed by Mn 3d and are also the source of

electrical conduction in $Mn_{23}C_6$. There are no covalent bonds observed between Mn–C or C–C atoms, which means that it lacks the common covalent bond network like other carbides. Combined with the calculated Bader charge, each C atom receives 0.24 electrons on average from Mn_{II} and Mn_{IV} atoms, therefore, the Mn–C bond is ionic and specific only in Mn_{II}–C and Mn_{IV}–C. The Mn–Mn bond is metallic, and there are no electrons transfer within the Mn–Mn bonds, which also proves that the Mn 3d electron is the source of electrical conduction in $Mn_{23}C_6$.

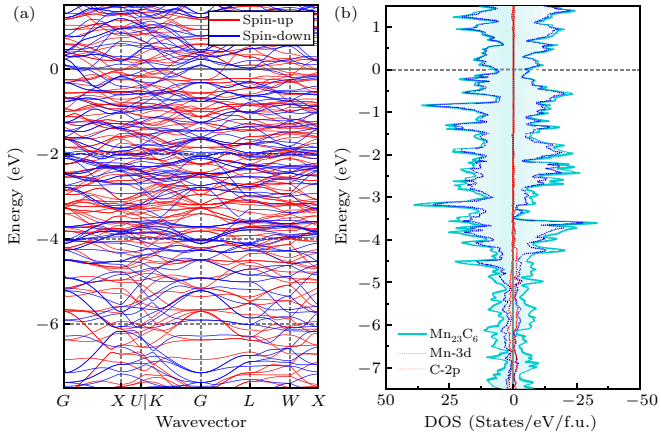


Fig. 5. Calculated energy band structure and density of states of $Mn_{23}C_6$: (a) energy band structure in a series of high order symmetry points, the red line and blue line are spin-up and spin-down bands, respectively; (b) partial density of states, cyan solid line, blue and red dashed lines are TDOS, Mn 3d PDOS and C 2p PDOS, respectively. The positive and negative represent the upper and lower spins of Mn 3d and C 2p electrons.

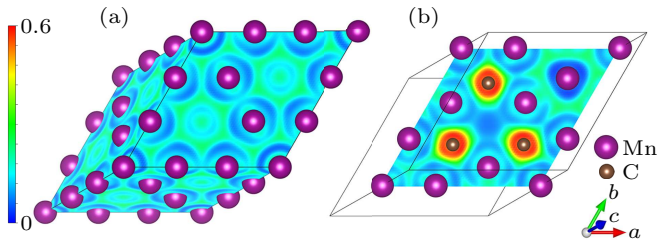


Fig. 6. Calculated electron localization function of $Mn_{23}C_6$. (a) The exterior and (b) 2D plots of a $Mn_{23}C_6$ unit cell and its (001) crystallographic plane.

To investigate the orbital hybridization and bonding situation between Mn and C atoms, in Fig. 7(a), the bonding information of $Mn_{23}C_6$ can be obtained by the calculated projected crystal orbital Hamilton population (COHP). In $Mn_{23}C_6$, the interatomic bonding within the crystal structure can be categorized into three types: Mn–Mn, C–C and Mn–C. In Fig. 7(a), the spin-up and spin-down of Mn–Mn bonds are both stabilized from 0 to −5 eV, meanwhile, the spin-up and spin-down are separate, these means the coexist of ferromagnetism and antiferromagnetism between Mn and Mn atoms, and this conclusion is the same as the *M*–*T* measurements in the experiment. The spin-up and spin-down pCOHP of Mn–Mn bonds around the Fermi level are both destabilized, which means that the Mn–Mn bonding electrons at the Fermi level are itinerant, these itinerant electrons also contribute to the high state density of Mn atoms in DOS near the Fermi level. Compared with Mn–Mn and Mn–C, the spin-up and spin-down pCOHP of C–C bonds are both very weak in the whole energy range, which is the same as the ICOHP results (see Table S3 in the supplementary material). This is due to the natural crystal structure character of $Mn_{23}C_6$, C atoms are dispersive in $Mn_{23}C_6$ crystal, thus C–C bonds cannot form interactions. The spin-up and spin-down pCOHP of Mn–C bonds are both stabilized from −5 eV to −8 eV, this energy range is the same as the p–d orbital hybridization in DOS. In addition, the Mn–C bonds have the highest ICOHP in Table S3, which proves that the p–d orbital hybridization in Mn–C is the main bonds in $Mn_{23}C_6$. The spin-up curve and spin-down curve of Mn–C bonds are similar from −5 eV to −8 eV, this means the magnetic order of Mn–C is antiferromagnetic coupling. Combining with the above calculated results, we could draw a conclusion that owing to that the Mn 3d is approximately half-filled and it provides abundant DOS around E_F, Mn 3d electrons have a great influence on the electromagnetic properties of $Mn_{23}C_6$. In addition, we also should not ignore the influence of p–d orbital hybridization between Mn and C atoms, because C 2p influences Mn 3d by bonding and electron transfer. To figure out the inside magnetic order and its mechanism in $Mn_{23}C_6$, we calculate the spin-polarized electrons of the (110) and (01$\bar{1}$) crystallographic planes in an $Mn_{23}C_6$ unit cell and the results are shown in Figs. 7(b) and 7(c), respectively. In Fig. 7(b), Mn and C atoms are typical antiferromagnetic coupling based on the indirect super-exchange interaction, the calculated magnetic moment (see Table S2 in the supplementary material) of Mn atoms is $1.56\mu_B$, close to the experimental magnetic moment $\mu_{eff} = 1.46 \pm 0.02\ \mu_B$ as measured by neutron diffraction.[17] The calculated value is slightly higher than the experimental one because the initial magnetic structure in calculation is ferromagnetic. However, both the experimental measurements in this paper and previous works confirm that the magnetic order of $Mn_{23}C_6$ should not be so simple as an antiferromagnetism. We should note that Mn atoms are not spin-up and their magnetic moments are variational in Table S2. Thus, we also study the magnetic order of different crystallographic planes and find that there is another magnetic order. As shown in Fig. 7(c), except the above Mn–C antiferromagnetic indirect super-exchange interaction, there is also Mn–Mn antiferromagnetic direct exchange interaction along the [01$\bar{1}$] zone axis, the two spin-down Mn atoms in Fig. 7(c) correspond to the only two spin-down Mn atoms (Mn2 and Mn3) in Table S2, and these spin-down Mn atoms show the strongest magnetic moment about $-3.250\mu_B$. Combining with the random distribution of each Mn atomic magnetic moment and the above research results, we conclude that the reason for this is the competition between the two magnetic interactions in $Mn_{23}C_6$. In this work, we have also solved the decades-old problem of the

true magnetic order of $Mn_{23}C_6$, the magnetic order of $Mn_{23}C_6$ is actually composed of both Mn–C antiferromagnetic indirect super-exchange interaction and Mn–Mn antiferromagnetic direct exchange interaction, the competition between these two interactions also leads to the spin frustration, the net magnetic moment and M–T curves bifurcation at low temperature.

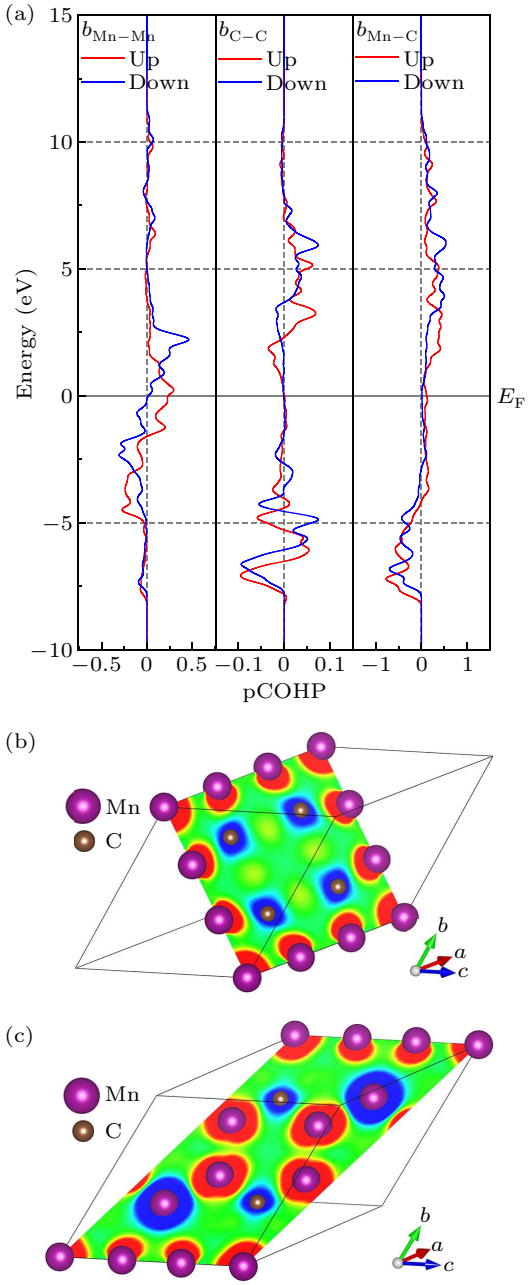


Fig. 7. Calculated bonds characteristic and spin-polarized electron of $Mn_{23}C_6$: (a) projected crystal orbital Hamilton population for Mn–Mn bonds, C–C bonds and Mn–C bonds, positive COHP values denote bonding and negative COHP values denote antibonding; (b) and (c) the spin-polarized electron plots of (110) and (01$\bar{1}$) crystallographic planes, respectively. Red and blue areas mean spin-up and spin-down electrons.

5. Concluding remarks and perspectives

In summary, we synthesized high-quality bulk $Mn_{23}C_6$ at 5.0 GPa and 1200 K using HTHPQM and demonstrated its structural, mechanical and electromagnetic properties in this work. The bulk $Mn_{23}C_6$ is polycrystalline, single-phase and has an FCC structure with space group *Fm*-3*m* (No. 225), $D8_4$ strukturbericht symbolism structure. Our characterization shows that the sample is of high density (95.74%), good conductivity (8.47×10^{-4} Ω·m), antiferromagnetism with its Néel temperature $T_N = 104$ K, homogeneous and its average grain sizes are 2–15 μm. Moreover, we confirmed and solved the long-standing question of the actual magnetic order of $Mn_{23}C_6$. According to our results, the antiferromagnetic $Mn_{23}C_6$ sample has two different antiferromagnetic exchange interactions simultaneously, one is the super-exchange interaction between Mn (except Mn_{III}) and C atoms, and the other one is the direct exchange interaction between Mn_{III} and the surrounding Mn atoms along the [01$\bar{1}$] zone axis. Similar to the magnetic cluster or spin frustration system, this ferromagnetic–antiferromagnetic competition between these two interactions leads to the net magnetic moment and M–T curves bifurcation at low temperature. These conclusions not only apply to $Mn_{23}C_6$, as a typical IMC, but also help understanding the magnetic mechanisms of other carbides of $Mn_{23}C_6$-type.

Acknowledgments

This work was partially carried out at Instrument sharing platform of College of Physics in Jilin University. Parts of the calculations were performed in the High Performance Computing Center (HPCC) of Jilin University.

References

[1] Yu C C, Wu H J, Agne M T, Witting I T, Deng P Y, Snyder G J and Chu J P 2019 *APL Materials* **7** 013001
[2] Wang Y X, Yao J H and Li Y J 2018 *Mater. Sci. Technol.* **34** 605
[3] Xiao B, Xing J D, Feng J, Zhou C T, Li Y F, Su W, Xie X J and Cheng Y H 2009 *J. Phys. D: Appl. Phys.* **42** 115415
[4] Karen P, Fjellvåg H, Kjekshus A and Andresen P 1991 *Acta Chemica Scandinavica* **45** 549
[5] Wu Y, Ma L S, Zhou X L, Duan Y H, Shen L and Peng M J 2022 *International Journal of Refractory Metals and Hard Materials* **109** 105985
[6] Inoue A and Masumoto T 1980 *Metallurgical Transactions A* **11** 739
[7] Jones W B, Hills C and Polonis D 1911 *Metallurgical Transactions A* **22** 1049
[8] Thomson R and Bhadeshia H 1992 *Metallurgical Transactions A* **23** 1171
[9] Zhang Y, Wang Y H, Huang J J, Han C and Zang J B 2020 *International Journal of Hydrogen Energy* **45** 6529
[10] Xu B, Cui J J, Li M S, Li C M, Chu F M and Feng L M 2005 *Chin. Phys. Lett.* **22** 478
[11] Morgan E 1954 *JOM* **6** 983
[12] Benz R, Elliott J F and Chipman J 1973 *Metallurgical Transactions* **4** 1449
[13] Benz R, Elliott J F and Chipman J 1973 *Metallurgical Transactions* **4** 1975
[14] Karen P and Hájek B 1986 *Collection of Czechoslovak Chemical Communications* **51** 1628
[15] Kim B, Yu K, Kim J, Kwon H, Lee S and Lee Y 2020 *Progress in Superconductivity and Cryogenics* **22** 62
[16] Kowalik I 2015 *Acta Phys. Pol. A* **127** 831
[17] Guchhait S, Ohldag H, Arenholz E, Ferrer D A, Mehta A and Banerjee S K 2013 *Phys. Rev. B* **88** 174425
[18] Hohenberg P and Kohn W 1964 *Phys. Rev.* **136** B864
[19] Larson A C and Von Dreele R B 1985 *Report lAUR* **86** 748

[20] Kresse G and Hafner J 1993 *Phys. Rev. B* **47** 558
[21] Kresse G and Furthmüller J 1996 *Phys. Rev. B* **54** 11169
[22] Kresse G and Furthmüller J 1996 *Comp. Mater. Sci.* **6** 15
[23] Teter M P, Payne M C and Allan D C 1989 *Phys. Rev. B* **40** 12255
[24] Perdew J P, Burke K and Ernzerhof M 1996 *Phys. Rev. Lett.* **77** 3865
[25] Monkhorst H J and Pack J D 1976 *Phys. Rev. B* **13** 5188
[26] Toby B H 2001 *Journal of Applied Crystallography* **34** 210
[27] Momma K and Izumi F 2008 *Journal of Applied Crystallography* **41** 653
[28] Bazargan A, Yan Y, Hui C W and McKay G 2013 *Ind. Eng. Chem. Res.* **52** 12689
[29] Ge Y F, Bao K, Ma T, Zhang J M, Zhou C, Ma S L, Tao Q, Zhu P Q and Cui T 2021 *ACS Omega* **6** 21436
[30] Ge Y F, Ma S L, Bao K, Tao Q, Zhao X B, Feng X K, Li L, Liu B, Zhu P W and Cui T 2019 *Inorg. Chem. Front.* **6** 1282
[31] Zhao X B, Bao K, Ma S L, Zhou C, Zhu P W, Tao Q and Cui T 2024 *J. Alloys Compd.* **982** 173800
[32] Yao L L, Si P Z, Ge H L, Qian H D and Choi C J 2019 *J. Electron. Mater.* **48** 1436
[33] Yatsuzuka H, Haraguchi Y, Matsuo A, Kindo K and Katori H A 2022 *Sci. Rep.* **12** 2429
[34] Ribeiro P R T, Machado F L A, Harrison D C, Dahlberg E D and Rezende S M 2022 *J. Magn. Magn. Mater.* **541** 168537
[35] Ma Z, Wang J H, Dong Z Y, *et al.* 2018 *Phys. Rev. Lett.* **120** 087201
[36] Niimi Y, Kimata M, Omori Y, Gu B, Ziman T, Maekawa S, Fert A and Otani Y 2015 *Phys. Rev. Lett.* **115** 196602